Chalcogenide Letters Vol. 21, No. 9, September 2024, p. 747 - 755

Influence of chromium concentration on the structural, optical, magnetical, and thermal properties of ZnS nanocrystals

R. Selvam[a], I. Devadoss[b,*], A. Krishnamoorthy[b], S. P. Sheeba[b]
[a]*Srinivasan College of Arts and Science (Affiliated to Bharathidasan University, Tiruchirappalli), Perambalur-621 212, Tamil Nadu, India*
[b]*PG & Research Department of Physics, Bishop Heber College (Affiliated to Bharathidasan University, Tiruchirappalli), Tiruchirappalli - 620 017, Tamilnadu, India*

Pure ZnS and $Zn_{1-x}Cr_xS$ nanoparticles were successfully prepared using the coprecipitation method, where x represents the concentration (x = 0.00, 0.10, and 0.05). There are many analytical methods used, such as X-ray diffraction (XRD), scanning electron microscopy (SEM), and Spectroscopy of energy dispersive (EDS). The magnetism structure of the catalysts was investigated using spectrophotometry (VSM), thermogravimetric analysis (TGA), and differential thermal analysis (DTA). X-ray diffraction studies determine the nanocrystal arrangement and size of microcrystals. As seen in SEM analysis, the particles are agglomerated. The coordination of sulfur ions around zinc ions was examined using FTIR analysis. The energy band gap of the Cr-doped sample increases. Photoluminescence spectroscopy showed that the violet emission around 424 nm could be attributed to the excitation process of electrons from the low energy of the conduction band to the valence band of sulfur intermediate atoms. The front amplitude of doped ZnS nanocrystals remains constant regardless of the amount of Cr present. The results show that the ZnS nanocrystals were replaced by dilute Cr^{3+} ions. Cr-doped ZnS exhibits diamagnetic properties under high-temperature conditions. The results show that these materials are improved by the Cr doping process, making them suitable for many applications.

(Received April, 8, 2024; Accepted September 18, 2024)

Keywords: Cr, ZnS, VSM, SEM, Diamagnetism, Nanocatalyst

1. Introduction

Advances in science and technology have been influenced by semiconductors. Recent advances in nanotechnology can create new smart and advanced devices [1,2]. These will have many applications in areas such as spintronics, cathode ray tubes, optical components, and anti-reflective coatings [3]. The excellent luminescent, magnetic, and optoelectronic properties of semiconductor nanocrystals have attracted the attention of the scientific and technological community and made them the best products for research development. Current research focuses on developing new magnetic materials for new devices and new designs for solid-state devices [4]. Such devices are best made using wide bandgap semiconductor materials. The reduced toxicity of semiconductors makes them useful in many coating applications, in addition to their broad research and commercial importance [5]. Sulfides and selenides have recently emerged as the most interesting materials in the semiconductor family due to their great potential in many fields such as optoelectronic devices, light-emitting diodes, optical sensors, photovoltaic devices, medical diagnostics, biomarkers, solar energy conversion [6,7]. ZnS comes in two crystal forms with slightly different bandgap energies and is one of the best n-type semiconductors [8]. One of them is a room-temperature metastable cubic zinc alloy structure with space group F-4m (216); The other is the thermodynamically stable hexagonal wurtzite structure with the P6-3 mc space group [9]. In terms of room temperature stability, the cubic zinc alloy structure is superior to the hexagonal wurtzite structure. The excellent thermochemical stability of ZnS may enable the use of electronic nanodevices, sensors, nanogenerators, and anti-reflective coatings. Inorganic semiconductor nanocrystals can be doped with transition metal ions to improve their optical, electrical, magnetic, and physical properties [10,11]. Among the transition metals, chromium can exhibit high magnetic moments and a wide

* Corresponding author: selvamr148@gmail.com
https://doi.org/10.15251/CL.2024.219.747

range of oxidation states. The development of lightweight and ferromagnetic materials is greatly influenced by chromium ions, which are more stable than other materials [12]. Chen et al [13]. Chawla et al [14]. They found that Cr-doped ZnS nanocrystals exhibited paramagnetic behaviour. Superparamagnetic behaviour was found in the same nanoparticles. Later, Kaur et al [15]. found that chromium-doped ZnS nanoparticles exhibited moderate ferromagnetism. and Purnaprakash et al [16]. These findings provide light on the weak magnetic properties of ZnS systems doped with chromium ions. However, next-gen spin-based devices necessitate wide bandgap semiconductors with improved magnetic characteristics. In light of this, we have achieved a significant improvement in the magnetic characteristics of Cr ions doped ZnS nanocrystals compared to earlier findings. Due to the fact that it is a transition element with several valences and has the potential to have a significant magnetic moment, Cr is an attractive dopant that may be used in optical and magnetic applications. The Cr-doped Al_2O_3 crystal was the first form of crystal to be used for laser emission. Furthermore, when the value of x reached 0.2, Satio et al. discovered that $Zn_xCr_{1x}Te$ exhibited ferromagnetism at normal temperature, with a Curie temperature estimated to be 300±6 at 10 K. In addition, Droubay et al. discovered that Cr-doped TiO_2 films exhibited ferromagnetism even when the temperature was at normal temperature. It is remarkable that there has been so little study done on Cr-doped ZnS. As a consequence of this, the primary objective of this research is to investigate Cr-doped ZnS nano semiconductor systems in order to produce distinctive optical and magnetic characteristics. Crystal structure, morphology, bonding nature, and optical and magnetic behaviors are elucidated through the systematic characterization of the structural, morphological, optical, thermal, and magnetic properties of Pristine and Cr ions doped ZnS nanocrystals in the present study.

2. Materials and methods

During the process of synthesis and study, the following chemicals were utilized from Merck: zinc acetate dihydrate ($Zn(CH_3CO2)2{\cdot}2H2O$), chromium nitrate trihydrate ($Cr(NO3)3.3H2O$), sodium sulfide (Na2S), ethanol (C2H5OH), and distilled water. Only reagents of an analytical grade are utilized in the synthesis and investigations that we conduct. The sodium sulphur (Na2S) should be dissolved in one hundred milliliters of distilled water. Next, dissolve one hundred milliliters of zinc acetate dihydrate in water. First, the two solutions were combined and agitated for five hours to produce pure ZnS nanoparticles. The synthesis of ZnS nanoparticles proved to be successful, producing a white cloudy solution. Finally, the obtained nanoparticles were dried in a vacuum oven at 50 degrees Celsius for 12 hours. The powder is dried and ground into a white powder that is pure zinc sulfide. Zn1-xCrxS nanocrystals produced using the synthesis process described above are represented by the names Zn0.95Cr0.05S and Zn0.90Cr0.10S. The powder is dried and ground into a white powder that is pure zinc sulfide. To make a powder that is light gray and contains Cr-doped ZnS, the powder is ground.

3. Results and discussion

3.1. Characterization

The synthesized nanocatalysts were characterized using an X-ray diffractometer equipped with CuKα radiation (λ = 1.5406 Å) at room temperature. We used a scan rate of 10°/min and a step size of 0.02°/2θ to record XRD patterns from 20° to 80. The voltage and current used to operate the detector are 200 kV and 12 μA, respectively. Fourier transform infrared spectroscopy studies were performed on a Perkin Elmer instrument by mixing the sample with appropriate amounts of KBr. Absorption spectra were obtained with a Perkin Elmer instrument with the step size set to 1 nm. Mix the sample with double distilled water and mix well. PL emission measurements were performed on powdered NC samples at room temperature on an Edinburgh spectrofluorometer using a 450 W xenon flash lamp, an HS RED PMT detector, and an integration time of 1s.

3.2. XRD analysis

Figure 1 shows the X-ray diffraction (XRD) patterns of pure ZnS and Cr-doped ZnS nanocrystals at different concentrations. Measurements were taken in the range of 0 to 80^0. Data level analysis was performed according to standard JCPDS Card No. 05-0566[17]. At 2θ values, three distinct and extended diffraction peaks are observed at 28.65º, 48.13º and 56.39º. These peaks correspond to the (111), (220), and (311) orientations of cubic ZnS, respectively. The most important difference occurs in the (111) direction. The broadening of the signal peaks indicates the size of the nanoparticle crystallites [18,19]. After the introduction of Cr doping, both the peak width and full width at half maximum (FWHM) gradually increased. A small shift towards higher diffraction angles was also detected. The observed increase in difference angle can be attributed to the lattice shrinkage

caused by the smaller Cr ion radius (0.63 Å) compared to the Zn ion radius (0.74 Å). This shows that Cr^{3+} effectively replaces Zn^{2+} ions in the ZnS lattice without changing the cubic structure of ZnS. X-ray diffraction (XRD) peaks are broadened due to the nanocrystalline structure of the material. The average crystallite size was determined using the Debye–Scherrer equation (1), and the average size of the synthetic particles was 51, 39, and 34 nm, respectively.

$$D = K\lambda / \beta Cos\theta \quad (1)$$

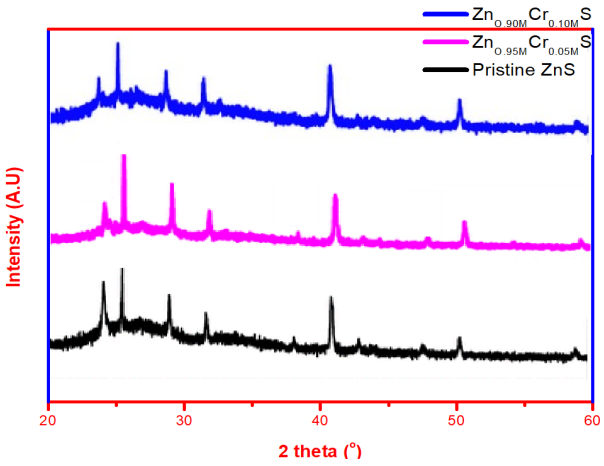

Fig. 1. XRD Analysis of pristine ZnS and various concentrations of Cr-doped ZnS NCs.

3.3. SEM/EDAX analysis

Experiments using SEM and XRD revealed the high purity of ZnS nanocrystals. The surface properties of zinc sulfide (ZnS) composites at different concentrations are shown in Figure 2(a, b, c). In addition to the presence of particle agglomeration in nanocrystals, a homogeneous distribution of particles with granular morphology was also found [20,21]. When particles are bonded together, it is difficult to break them into smaller particles. Some link together to form larger groups. As shown in Figure 2 (d, e, and f), the EDS spectra of pure ZnS and Cr-doped ZnS NCs at different concentrations are shown. Spectra of all strong peaks corresponding to zinc (Zn) and sulfur (S) in ZnS nanomaterials synthesized with different sulfur content. Table 1 shows EDAX analysis of synthesized nanomaterials.

Table 1. EDAX analysis of pristine ZnS and Various concentrations of Cr doped ZnS NCs.

Element	**Weight %**	**Atomic %**
S K	26.76	36.69
Zn K	73.24	63.31
Total	100	
Element	**Weight %**	**Atomic %**
S K	25.89	34.37
Cr K	1.86	3.5
Zn K	72.25	62.13
Total	100	
Element	**Weight %**	**Atomic %**
S K	25.8	32.56
Cr K	2.72	4.11
Zn K	71.48	63.33
Total	100	

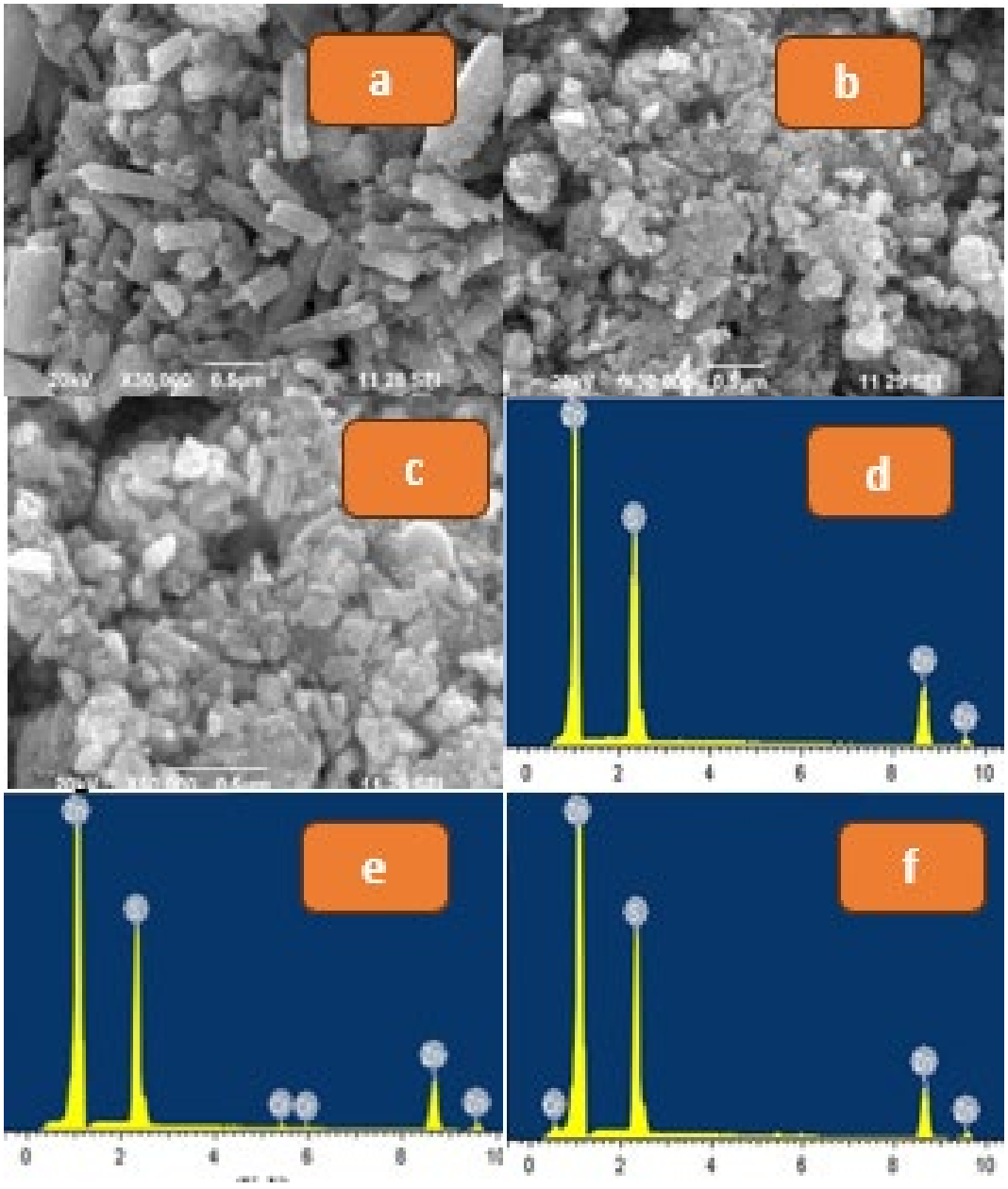

Fig. 2. SEM and EDAX Analysis of Pristine ZnS and Various concentrations of Cr doped ZnS NCs.

3.4. Ultraviolet-visible spectroscopy

Figure 3 illustrates the UV Spectrum and bandgap computation for Pristine ZnS and Various concentrations of Cr-doped ZnS Nanocrystals under Ultra-violet Spectroscopy. Upon comparison with pristine ZnS, the absorption edge of $Zn_{0.95}Cr_{0.05}S$ and $Zn_{0.90}Cr_{0.10}S$ NPs was meagrely towards the longer wavelength with redshift, it was attributed to the tiny changes in the particle size with rising Cr concentration. The absorption peaks of the synthesized nanocrystals were 293 nm, 306 nm, and 310 nm respectively, they are red-shifted with regard to the bulk ZnS absorption edge as a result of the quantum confinement effect they exhibit. It is important to note that the slope of the absorption edge becomes flatter as the concentration of Cr increases. This flattening out may be attributed to the increasing number of lattice defects that are created by the doping of the material with Cr. These peak variations are seen in ZnS nanocrystallites that have been doped with Cr as opposed to ZnS nanocrystallites that have not been doped with Cr, and the absorption intensities of these changes increase as the concentration of Cr rises. The bandgap of different ratios of Cr doped ZnS NPs were calculated using the equation [22,23],

$$(\alpha hv)n = A(hv - Eg) \quad (2)$$

The band gap values found in prepared NCs were 3.01 e,V, 3.09 eV, They are red-shifted with regard to the bulk ZnS absorption edge as a result of the quantum confinement effect they exhibit. For more information, it is important to note that the slope of the absorption edge becomes flatter as the concentration of Cr increases. This flattening out may be attributed to the increasing number of lattice defects that are created by the doping of the material with Cr. These peak variations are seen in ZnS nanocrystallites that have been doped with Cr as opposed to ZnS nanocrystallites that have not been doped with Cr, and the absorption intensities of these changes increase as the concentration of Cr rises. results in the increasing band gap. This was attributed to the bulk CrS with 2.4 eV as the band gap which was larger than that of pristine ZnS with 3.6 eV as band gap[24,25].

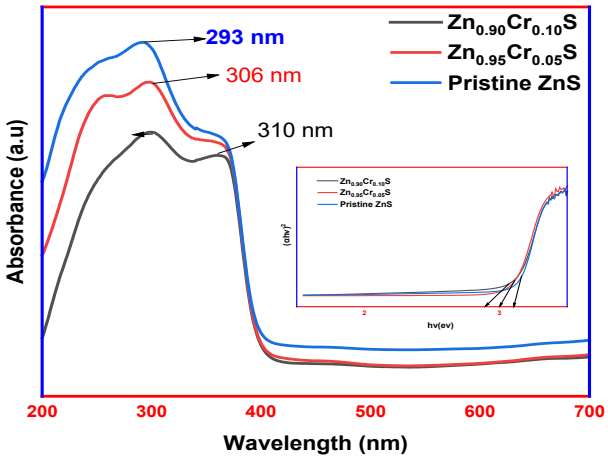

Fig. 3. UV-Visible and bandgap analysis of pristine ZnS and various concentrations of Cr doped ZnS N.

3.5. Photoluminescence

Photoluminescence (PL) refers to the light that a material emits when exposed to light. Figure 4 shows the photoluminescence (PL) spectra of ZnS nanoparticles with different Cr concentrations. These nanoparticles were produced by incorporation of Cr into ZnS and excited at wavelengths of 356 nm, 358 nm, and 357 nm at ambient temperature. Photoluminescence spectra showed distinct violet emission bands at 385 nm, 386 nm, and 389 nm, respectively. This band is pushed towards the red end of the visible spectrum. The emission can be attributed to defective energy levels in the ZnS lattice. Purple emission with a wavelength of 424 nm results from the release of electrons from the lower energy level of the conduction band into the valence band of sulfur interstitial atoms. The transition is approximately 3.05 electron volts below the conduction band limit. The strong violet emission at 431 nm is attributed to the transition of the electron beam to the zinc gap energy level.

3.6. Fourier Transform Infrared Spectroscopy (FTIR)

Figure 5 shows the FTIR spectra of ZnS nanoparticles containing different amounts of Cr. The broad band observed in the spectrum around 3500 cm^{-1} can be attributed to the O-H stretching frequency vibrations of the water molecules present. The peak seen in the wavenumber range from 1300 to 1600 cm^{-1} can be attributed to the presence of interlayer nitrate. The presence of mixed oxide deposits leads to a peak between 650 and 850 cm^{-1}. The formation of the Zn-S bond is attributed to the band gap of 562 cm^{-1} for pure ZnS. The stretching frequency of Cr-doped ZnS nanoparticles increases with the Cr content in ZnS. The stretching frequency of chromium-doped zinc sulfide nanoparticles (Cr-doped ZnS NPs) exhibits a larger change. Specifically, for 0.10M ($Cr_{0.10}M$) chromium concentration, the stretching frequency is found at 568cm-1, while for 0.05M ($Cr_{0.05}M$) chromium concentration, the stretching frequency is found at 572cm-1. Chromium atoms have a

smaller size than zinc atoms. According to the current vibration mode theory, changing the material in the composite material should cause movement. The frequency shift confirms the incorporation of Cr ions into the ZnS system.

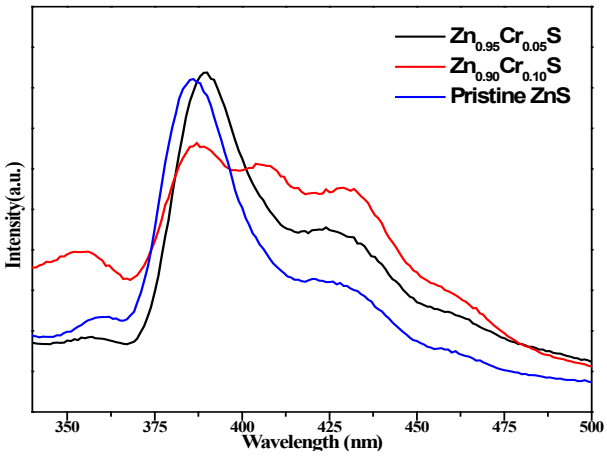

Fig. 4. PL Analysis of pristine ZnS and various concentrations of Cr-doped ZnS NCs.

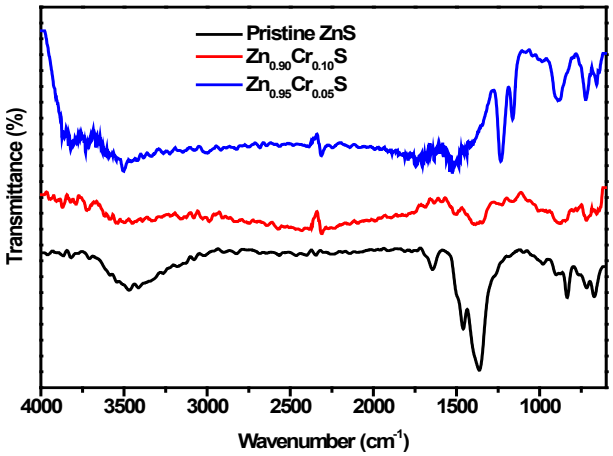

Fig. 5. FTIR analysis of pristine ZnS and various concentrations of Cr doped ZnS NCs.

3.7. TGA analysis

Thermogravimetric analysis plays a crucial role in assessing the thermal stability of materials. Figures 6(a) and (b) display the TGA and DTA curves of ZnS and different concentrations of chromium-doped ZnS nanostructures. The ZnS nanocrystals doped with Cr^{3+} ions exhibit three distinct stages of weight reduction as demonstrated in Thermogravimetric Analysis (TGA). Additionally, three endothermic peaks are detected in Differential Thermal Analysis (DTA). The TGA curve shows a weight loss of 9.5%, 10.38%, and 11.97% at a temperature of 99°C, which is likely caused by the evaporation of water that is physically absorbed by the host matrix. Three peaks exhibiting endothermic behaviour may be noticed on the DTA curve, occurring before a temperature of 600°C. At a temperature of 301° C, the chromium ions undergo breakdown, resulting in a weight loss of 13.21% from the ZnS matrix. The observed peak at a temperature of 508^0C is indicative of the endothermic process of material melting. The corresponding weight loss percentages are 16.32%, 17.25%, and 18.62% respectively. The additional wide endothermic peak observed at approximately 670° C can be ascribed to the slow depletion of remaining sulphur ions from the specimen. An overall weight reduction of 54.75% is found when the temperature is increased from room temperature to 110^0 C.

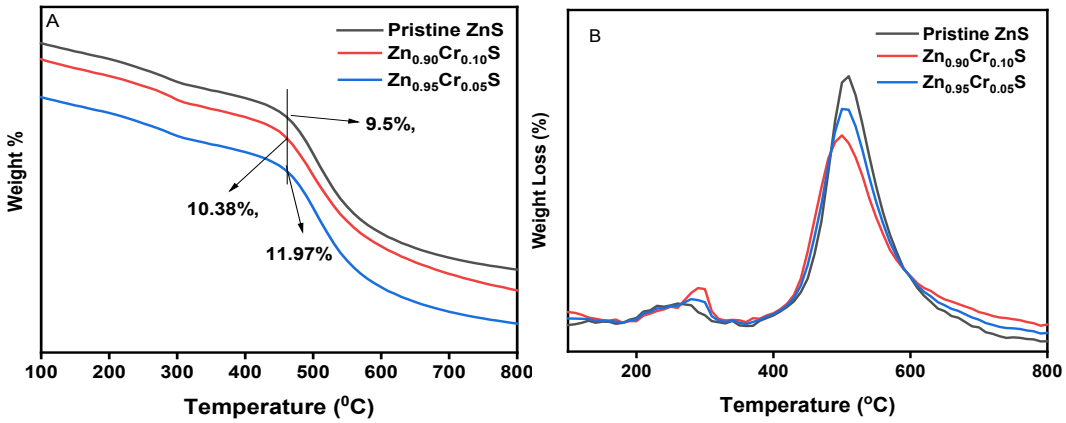

Fig. 6. (a) TGA and (b) DTA analysis of pristine ZnS and various concentrations of Cr doped ZnS NCs.

3.8. VSM analysis

A vibrating sample magnetometer (VSM) operating at 298 Kelvin is seen in Figure 6. This magnetometer was used to evaluate the magnetic characteristics of pure zinc sulphide (ZnS) as well as ZnS nanostructures that were doped with various quantities of chromium. It was discovered that the saturation magnetization values for ZnS were 75.61 emu/g, whereas the values for Cr0.05Zn0.95S were 64.63 emu/g, and the values for Cr0.10Zn0.90S were 61.96 emu/g. Zinc, the host metal, has a diamagnetic activity that is typical of the element. This behaviour may be explained by the fact that the d orbital of zinc does not contain any unpaired electrons. Since the samples of Cr-doped ZnS nanoparticles display straight lines, the figure makes it abundantly evident that these nanoparticles exhibit paramagnetic behaviour when they are at normal temperature. It is possible for theoretical ab initio calculations to provide an explanation for the non-ferromagnetism seen in ZnS nanoparticles that have been doped with Cr in this specific case. The ZnS lattice has Cr 3d states that are composed of an e doublet and a t2 triplet, and they possess a cubic crystal field. These states are separated into two distinct states. The e levels have a lower level of energy as compared to the t2 levels. The coupling cannot take place since all of the t2 levels are now occupied, hence there is no room available for it. In spite of this, ferromagnetism is a possibility when there is a double exchange taking place via the localised holes.

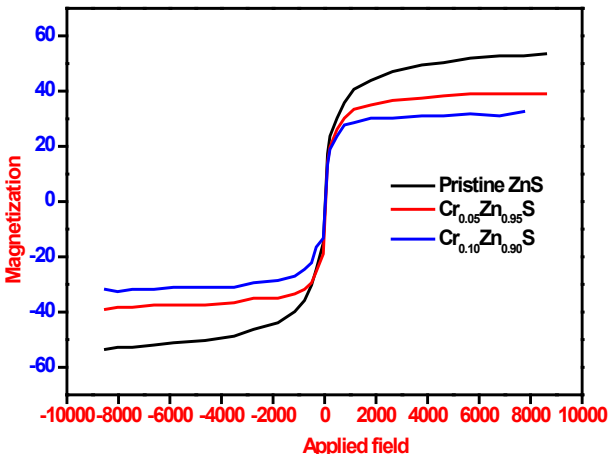

Fig. 7. VSM analysis of pristine ZnS and various concentrations of Cr doped ZnS NCs.

4. Conclusion

Cr ions doped ZnS nanocrystals were effectively synthesized utilizing the precipitation method, resulting in an average particle size of less than 34 nm, without the use of any capping agents. The morphological analysis revealed particles that were consistently dispersed and had granular forms, as well as particle agglomerations. The UV-Vis experiments revealed that the Cr-ZnS NCs exhibited a little shift towards longer wavelengths, known as a redshift. This shift was ascribed to the small variations in particle size that occurred as the concentration of Cr increased. The PL analysis reveals two distinct violet light emission bands for Cr-ZnS, both of which are red-shifted within the visible range. The stability of ZnS nanocrystals doped with Cr3+ ions was determined using TGA and DTA analysis. The obtained results will provide valuable insights for investigating the utilization of ZnS nanocrystals doped with Cr3+ ions in spintronics and nanoscale quantum devices. Additionally, these nanocrystals displayed ferromagnetic properties at ambient temperature.

References

[1] Pandey, P. (2022), Recent Patents on Nanotechnology, 16(1), 45-66; https://doi.org/10.2174/1872210515666210120114504
[2] Pyo, S., Lee, J., Bae, K., Sim, S., Kim, J. (2021), Advanced Materials, 33(47), 2005902; https://doi.org/10.1002/adma.202005902
[3] Baisnab, D. K., Mukherjee, S., Das, S. (2021), Chemical Solution Synthesis for Materials Design and Thin Film Device Applications, 231-275; https://doi.org/10.1016/B978-0-12-819718-9.00007-8
[4] Sivakumar, M., Kanakarajan, P., Jeevanantham, V. (2024), Journal of Ovonic Research, 20(2), 201-207; https://doi.org/10.15251/jor.2024.202.201
[4] Terna, A. D., Elemike, E. E., Mbonu, J. I., Osafile, O. E., Ezeani, R. O. (2021), Materials Science and Engineering: B, 272, 115363; https://doi.org/10.1016/j.mseb.2021.115363
[5] Wang, J., Dong, J. (2020), Sensors, 20(14), 3981; https://doi.org/10.3390/s20143981
[6] Kim, H. J., Sritandi, W., Xiong, Z., Ho, J. S. (2023), Biophysics Reviews, 4(1); https://doi.org/10.1063/5.0102811
[7] Shah, S. S. A., Awan, S. U., Zainab, S., Tariq, H., Riaz, M. B., Ul-Haq, A., Iqbal, N. (2023), Optical Materials, 141, 113816; https://doi.org/10.1016/j.optmat.2023.113816
[8] Yamçiçier, Ç., Kürkçü, C., & Merdan, Z. (2020), Solid State Sciences, 105, 106209; https://doi.org/10.1016/j.solidstatesciences.2020.106209
[9] Wang, H., Liang, X., Wang, J., Jiao, S., Xue, D. (2020), Nanoscale, 12(1), 14-42; https://doi.org/10.1039/C9NR07008G
[10] Jagadeeswari, R., Selvakumar, P., Jeevanantham, V., Saravanan, R. (2021), Archives of Metallurgy and Materials, 66(3), 911-915. https://doi.org/10.24425/amm.2021.136397
[11] Elahi, E., Dastgeer, G., Nazir, G., Nisar, S., Bashir, M., Qureshi, H. A. Imran, M. (2022), Computational Materials Science, 213, 111670; https://doi.org/10.1016/j.commatsci.2022.111670
[12] Chen, X., Wang, T., Han, Y., Lv, W., Li, B., Su, C., Yang, Z. (2021), Sensors and Actuators B: Chemical, 345, 130423; https://doi.org/10.1016/j.snb.2021.130423
[13] Ramalingam, G., Magdalane, C. M., Kumar, B. A., Yuvakkumar, R., Ravi, G., Jothi, A. I., Ananth, A. (2022); Environmental Research, 203, 111855; https://doi.org/10.1016/j.envres.2021.111855
[14] Shakila, P. B., Jeevanantham, V., Nagalakshmi, R., & Saravanan, R. (2023), Biomass Conversion and Biorefinery, 1-11. https://doi.org/10.1007/s13399-023-04793-7
[15] Poornaprakash, B., Chalapathi, U., Poojitha, P. T., Vattikuti, S. P., Park, S. H. (2019). Materials Science in Semiconductor Processing, 100, 73-78; https://doi.org/10.1016/j.mssp.2019.04.043
[16] Sathya, V., Jagatheesan, R., Jeevanantham, V., Gopi, D., Baby Shakila, P. (2023), *53*(9), 1887-1894. https://doi.org/10.1007/s10800-023-01890-3

[17] Gopinatha, P., Suresh, P., & Jeevanantham, V. (2023), Journal of Ovonic Research, 19(1). 23-30; https://doi.org/10.15251/JOR.2023.191.23
[18] Voigt, D., Sarpong, L., Bredol, M. (2020), Materials, 13(18), 4162; https://doi.org/10.3390/ma13184162
[19] Keerthana, M., Malini, T. P., Kamaraj, P., Vivekanand, P. A., Arulnangai, R., Kumar, S. J. S., Perumal, K. (2023). Journal of the Taiwan Institute of Chemical Engineers, 105118. https://doi.org/10.1007/s44371-024-00020-y
[20] Saravanan, P., K. Srinivasa Rao, M. Premkumar, A. K. Singh, Journal of alloys and compounds 509, no. 9 (2011): 3880-3885; https://doi.org/10.1016/j.jallcom.2010.12.141
[21] Aqeel, M., Ikram, M., Asghar, A., Haider, A., Ul-Hamid, A., Naz, M., Ali, S. (2020), Applied Nanoscience, 10, 2045-2055; https://doi.org/10.1007/s13204-020-01268-3
[22] Jini, D., Aravind, M., Ajitha, S., Parvathiraja, C., Muniyappan, M., Vivekanand, Arulnangai, R., P. A., Gonfa, G. (2022), Advances in Materials Science and Engineering, (1), 4020288. https://doi.org/10.1155/2022/4020288
[23] Nangai, R. A., Sihabudeen, M. M., Vivekanand, P. A., & Kamaraj, P. (2023), Malaya Journal of Matematik, 2, 2031-2036; https://doi.org/10.26637/mjm0s20/0525
[24] Kaur, M., Ubhi, M. K., Grewal, J. K., Singh, D. (2021), Journal of Physics and Chemistry of Solids, 154, 110060; https://doi.org/10.1016/j.jpcs.2021.110060